

# A concept of “materials” diffraction and imaging beamline for SKIF: Siberian circular photon source

Cite as: Rev. Sci. Instrum. **94**, 013305 (2023); <https://doi.org/10.1063/5.0103481>

Submitted: 16 June 2022 • Accepted: 09 December 2022 • Published Online: 13 January 2023

Vladimir A. Chernov,  Ivan A. Bataev,  Yakov V. Rakshun, et al.



[View Online](#)



[Export Citation](#)



[CrossMark](#)



**APL Energy**  
Bridging basic research and innovative  
technology that will impact the future  
**Now Open for Submissions**

# A concept of “materials” diffraction and imaging beamline for SKIF: Siberian circular photon source

Cite as: Rev. Sci. Instrum. 94, 013305 (2023); doi: 10.1063/5.0103481

Submitted: 16 June 2022 • Accepted: 9 December 2022 •

Published Online: 13 January 2023



View Online



Export Citation



CrossMark

Vladimir A. Chernov,<sup>1</sup> Ivan A. Bataev,<sup>2,a)</sup>  Yakov V. Rakshun,<sup>1,3</sup>  Yuri V. Khomyakov,<sup>1,4</sup>   
Maksim V. Gorbachev,<sup>2</sup>  Andrei E. Trebushinin,<sup>1</sup>  Nikolay I. Chkhalo,<sup>5</sup>  Dmitry A. Krasnorutskiy,<sup>2</sup>   
Viktor S. Naumkin,<sup>2,6</sup>  Artem N. Sklyarov,<sup>4</sup>  Nikolay A. Mezentsev,<sup>1</sup> Alexander M. Korsunsky,<sup>7</sup>   
and Igor P. Dolbnya<sup>8,a)</sup> 

## AFFILIATIONS

<sup>1</sup>Budker Institute of Nuclear Physics, 11 Acad. Lavrentyev Av., Novosibirsk 630090, Russian Federation

<sup>2</sup>Novosibirsk State Technical University, 20 Karl Marks Av., Novosibirsk 630073, Russian Federation

<sup>3</sup>Siberian State University of Telecommunications and Information Science, 86 Kirova Str., Novosibirsk 630102, Russian Federation

<sup>4</sup>Novosibirsk State University, 1 Pirogova Str., Novosibirsk 630090, Russian Federation

<sup>5</sup>Institute for Physics of Microstructures, Nizhny Novgorod 607680, Russian Federation

<sup>6</sup>Kutateladze Institute of Thermophysics, 1 Acad. Lavrentyev Av., Novosibirsk 630090, Russian Federation

<sup>7</sup>Department of Engineering Science, University of Oxford, Oxford OX1 3PJ, United Kingdom

<sup>8</sup>Diamond Light Source, Harwell Science and Innovation Campus, Didcot, Oxfordshire OX11 0DE, United Kingdom

<sup>a)</sup>Authors to whom correspondence should be addressed: [i.bataev@corp.nstu.ru](mailto:i.bataev@corp.nstu.ru) and [igor.dolbnya@diamond.ac.uk](mailto:igor.dolbnya@diamond.ac.uk)

## ABSTRACT

Over the next decade, the extremely brilliant fourth generation synchrotron radiation sources are set to become a key driving force in materials characterization and technology development. In this study, we present a conceptual design of a versatile “Materia” diffraction and imaging beamline for a low-emittance synchrotron radiation facility. The beamline was optimized for operation with three main principal delivery regimes: parallel collimated beam  $\sim 1$  mm beam size, micro-focus regime with  $\sim 10$   $\mu\text{m}$  beam spot size on the sample, and nano-focus regime with  $<100$  nm focus. All regimes will operate in the photon energy range of 10–30 keV with the key feature of the beamline being fast switching between them, as well as between the various realizations of diffraction and imaging operation modes while maintaining the target beam position at the sample, and with both spectrally narrow and spectrally broad beams up to the energy band  $\Delta E/E$  of  $5 \times 10^{-2}$ . The manuscript presents the details of the principal characteristics selected for the insertion device and beamline optics, the materials characterization techniques, including the simulations of thermal load impact on the critical beamline optics components. Significant efforts were made to design the monochromators to mitigate the very high beam power load produced by a superconducting undulator source. The manuscript will be of interest to research groups involved in the design of new synchrotron beamlines.

Published under an exclusive license by AIP Publishing. <https://doi.org/10.1063/5.0103481>

## I. INTRODUCTION

The fourth generation synchrotron radiation (SR) sources provide ultra-small emittance and extremely high brightness of x-radiation that open up new and exciting opportunities for studies of the structure and function of materials. The greatest benefit of the new fourth generation sources can be exploited using undulator beamlines that can deliver record-breaking photon flux and

small beam size on the sample. At present, there is a limited number of beamlines that utilize the full potential of the new sources for applications in materials science. In this context, one may mention the ID11 instrument at ESRF-EBS (France),<sup>1</sup> nanoMAX and DanMax beamlines at MAX-IV facility (Sweden),<sup>2</sup> the EMA beamline under construction at the SIRIUS synchrotron (Brazil),<sup>3</sup> among others. One of the important trends in designing modern beamlines is the attempt to combine several complementary experimental

techniques to enable the collection of simultaneous or collocated information.

X-ray diffraction (XRD) and imaging are two of the most requested experimental characterization modes in materials science, with the combination of both methods being of particular interest to materials scientists. Several modern beamlines are capable of offering both methods but not simultaneously. Typically, the combination is enabled by switching between the two modes. Generally, this requires a significant amount of time and effort. At the same time, the realization of such simultaneous combination could be of great benefit, similar to the “point and shoot” approach that has been used in electron microscopy for decades. It allows researchers to select a certain specimen point for the analysis of the chemical composition, diffraction of back-scattered electrons, secondary ion mass spectroscopy, etc. using the previously obtained image. However, for quite a while this approach was not implemented on SR beamlines. A notable exception is the recently built beamline K11 DIAD (Dual Imaging and Diffraction) at Diamond Light Source, UK,<sup>4</sup> where the relatively fast switching (up to 10 Hz) between imaging (presently only in 2D) and diffraction regimes is planned to be implemented by the angular splitting of the photon beam from a wiggler source. The approach presented here seeks to achieve the same objective in a different manner—by fast switching of the required optical elements between collimated and focused beams using small beams generated by undulators. To the best of our knowledge, this approach has not been realized nor proposed so far. This approach undoubtedly represents a key novelty aspect of our work.

The aim of this paper is to introduce and detail the concept of a flexible multipurpose beamline that provides imaging-guided materials characterization, and to present some results of the simulation of its performance. The beamline is designed for SKIF: Siberian Circular Photon Source facility. In this study, we present the estimated characteristics of the beam, calculation results, and photon beam ray-tracing simulations (flux and losses at sequential beamline optical elements and spatial beam characteristics at various sample positions), including the simulations of the associated heat load effects. The end-station equipment and expected beamline capabilities are described.

## II. OBJECTIVES

The atomic structure, phase constitution, chemical composition, type, and density of crystal lattice defects, as well as the spatial distribution of different components throughout the sample represent the most important information that determines material performance. Many modern materials such as nano-/microstructured alloys and composites can be inhomogeneous at different spatial scales (from a few nanometers to a few millimeters), which requires different approaches (e.g., real space vs reciprocal space characterization) and different beam spot sizes on the sample. For the purposes of fine-tuning the material properties and a comprehensive understanding of its structure and function, *in situ* approaches are becoming extremely popular in synchrotron materials science and involve the sample being probed directly during the processes it is subjected to under external influence. Therefore, materials scientists require a diverse set of flexible characterization instruments. In an ideal case, several experimental research techniques are combined

altogether within the same instrument to provide a set of complementary experimental data collected from the same point/region of interest inside the sample.

XRD and imaging are in the range of mostly requested experimental characterization techniques in materials science. That was considered while optimizing the parameters of the insertion device and designing the optical scheme of the entire beamline. Wherein, both monochromatic and so-called “pink” beams are of a great interest for XRD experiments, so it was decided to evaluate both beam modes in subsequent calculations.

Other techniques, such as small-angle and ultra-small-angle x-ray scattering (SAXS and USAXS), anomalous diffraction, x-ray fluorescence (XRF) spectroscopy, and XRF scanning micro/nano-probe, x-ray absorption fine structure (XAFS) spectroscopy, are considered as supplementary. In perspective, it is also possible to use the beamline for 3D-XRD, advanced x-ray microscopy, and microtomography in various forms (dark-field, phase-contrast, coherent diffraction imaging (CDI), and ptychography). For ptychography, the preservation of a partially coherent beam wavefront or minimizing the effects of its distortion is a particular challenge that places stringent requirements on the major beamline optics components such as monochromators and final focusing optics. It is important to avoid the appearance of undesirable speckles and fringes that can be introduced by optics imperfections (see, e.g., Ref. 21). To mitigate these effects, it is planned to use phase correctors wherever possible.<sup>22</sup>

The main feature of the proposed “Materia” beamline is the ability to combine imaging and diffraction techniques by switching between them within a relatively short period of time. The imaging techniques would allow us to visualize the structure in a very straightforward way and select a specific area (region of interest) on the sample for subsequent characterization; whereas the diffraction (as well as other supplementary techniques) provides an important information on the “fine” structure of the sample, such as, e.g., phase constitution, lattice defects, crystallographic orientation, etc. For this combined approach, we propose a single-beam solution, which provides a few characterization techniques instantly available at a reasonably fast time scale while switching between imaging and diffraction modes of beamline operation.

The beamline will operate in three main beam delivery regimes: ~1 mm size (with no focusing—parallel or collimated beam)—mainly for x-ray imaging, 10  $\mu\text{m}$  and <100 nm with focusing (mainly for XRD, SAXS, and USAXS). The distinctive feature of the beamline will be the ability to preserve the beam spot at the same point of a sample while changing (in a wide range) or scanning the photon beam energy or reconfiguring the major beamline optics.

To a claim, the beamline is assumed to work as a giant “materials science microscope” with a wide range of possibilities for a combination of diffraction, imaging, and spectroscopic methods, providing high spatial and temporal resolutions. Hence, significant requirements on both the insertion device and the beamline optics are imposed. It is necessary to provide spectrally narrow and spectrally wide beams, maintain high radiation fluxes, to form beams ranging in size from 1 mm down to 100 nm at one and the same point/area of the sample, to “hold” this point with the beamline optics during a series of various measurements, and at the same time to ensure a mitigation of thermal loads on principal optical elements.

We have proposed fairly flexible instrumental methods to manage that challenge—the following beamline optics scheme (see Sec. IV “Optics: general scheme”): the transfocator, double-mirror monochromator (DMM), and quadrupole-crystal monochromators (QCM) are in the optics hutch of the beamline, the final focus optics (compound refractive lens (CRL) and Kirkpatrick-Baez (KB) mirrors) in the experiments hutch.

The following operation modes of the beamline are suggested here:

- For traditional diffraction methods, a transfocator, DMM, and/or QCM in various combinations will be used. The insertion device will operate normally.
- For Laue diffraction, the insertion device will operate in the broadened harmonics generation mode, the main optical elements will be the transfocator, and/or DMM.
- For XAFS experiments, the insertion device will also operate in the broadened harmonics generation mode, the main optical elements will be the transfocator, DMM, and QCM.
- For microradiography methods, including microtomography and ptychography, the transfocator and DMM will be used. It is assumed that the main mode of operation of the insertion device is normal, but operation in the mode of generation of broadened harmonics is also possible.
- Transfocator, DMM, and QCM in various combinations will be used for SAXS and USAXS, with the transfocator device operating in normal (beam collimating) regime.
- X-ray fluorescence analysis (XRF) is considered as an auxiliary research technique and can be easily implemented in conjunction with other methods by installing a semiconductor detector. Fluorescence confocal x-ray microscopy and microtomography are also planned.

It should be noted that DMM with different strips (see Sec. IV B) will be used in all the above modes. It is not assumed that the beamline will operate with the straight-through, primary (or “white”) beam. Preliminary collimation of radiation from the source will be provided by a set of fixed and adjustable masks placed in the front-end. For studies on the micrometer and sub-micrometer

scales, final focus optics (CRLs and/or KB mirrors) can be selectively inserted into the SR beam for all the experimental techniques.

To stress one important feature of the proposed scheme for applications in materials science research—in most operating modes of the optics the beam will be directed to the same point on the sample. In this case, switching between different modes of beamline operation (e.g., traditional and Laue diffraction) can be performed at a frequency of at least 1 Hz or more by controlled insertion and withdrawal of QCM channel-cut crystals from the beam. Changing the size of the focal spot using a transfocator is possible within times of about 0.1 s (or with a frequency of 10 Hz). Finally, the restructuring of the system between the diffraction and imaging methods is feasible within times of the order of 1 s (1 Hz). With the QCM, quick XAFS could be also implemented with data acquisition frequencies up to ~1 kHz.

In the following text, we report the extensive use of various simulation techniques. To aid clarity, we briefly explain the origin of the data used for the simulations. The input parameters of the accelerator were received from the developers of the SKIF synchrotron.<sup>6</sup> Superconducting undulator data were obtained from the calculations and preliminary results for the prototype produced at the Budker Institute of Nuclear Physics (Russia).<sup>23</sup> The parameters used for Be lenses in the transfocator and final focus CRL were obtained from RXOPTICS GmbH & Co. KG.<sup>4</sup> The positions of the optical elements and their sizes used for ray tracing simulations were obtained through iterative procedures to obtain optimal values. The choice of the parameters used for the thermal analysis of the monochromators is discussed in Sec. IV B 1.

### III. INSERTION DEVICE

The requirements for a high flux in the range of operational energies of 10–30 keV, small focused beam spot sizes (down to just a few hundreds of nanometers), and “pink” beam with a  $5 \cdot 10^{-2}$  bandwidth at energies of 15–25 keV can be fulfilled by implementing a two-section short-period superconducting undulator (SCU) as an insertion device (ID). The sections are to be joined by a three-pole phase compensator. The SCU is designed to operate at different

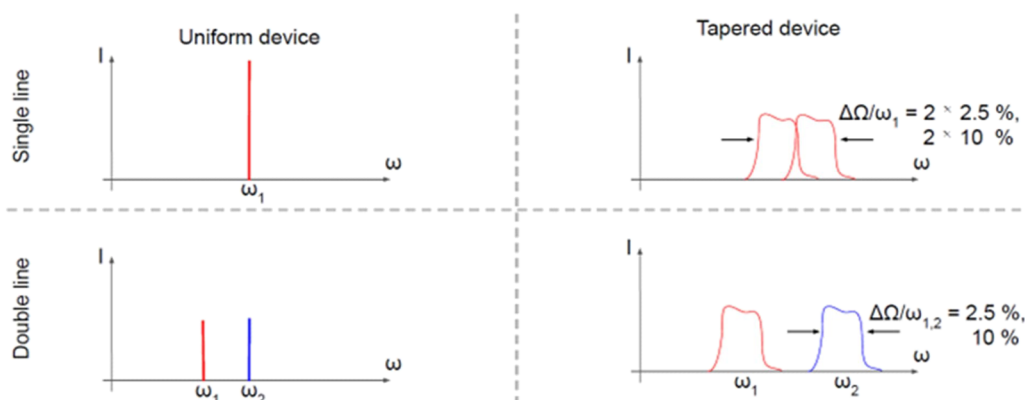


**FIG. 1.** Operational modes of the SCU. “Single line” means that the SCU sections operate with the same carrier frequency  $\omega_1$ ; “Double line” means that the SCU sections operate with slightly different carrier frequencies  $\omega_1$  and  $\omega_2$ .

**TABLE I.** Machine parameters of the “SKIF” storage ring and parameters of the superconducting undulator (SCU) for 400 mA beam current.  $\beta_x$  and  $\beta_y$  are presented for the corresponding straight sections of the storage ring.

Machine parameters		SCU parameters	
Energy	3 GeV	Period length	13.5 mm
Circumference	476.14 m	Number of periods	280
Beam current	400 mA	Peak field	1.08 T
No. of bunches	510	Magnetic gap	7 mm
Natural emittance	75 pm rad	Total (after mask and filter) radiation power	10 kW (286 W)
Coupling factor	10%	First harmonic	3285.92 eV
$\beta_x$	0.53 m	Low- $\beta$ source size (FWHM, 3rd harmonic)	18.3 $\mu\text{m}$ (H) $\times$ 15.4 $\mu\text{m}$ (V)
$\beta_y$	3.04 m	Low- $\beta$ source divergence (3rd harmonic)	14.3 $\mu\text{rad}$ (H) $\times$ 10.2 $\mu\text{rad}$ (V)

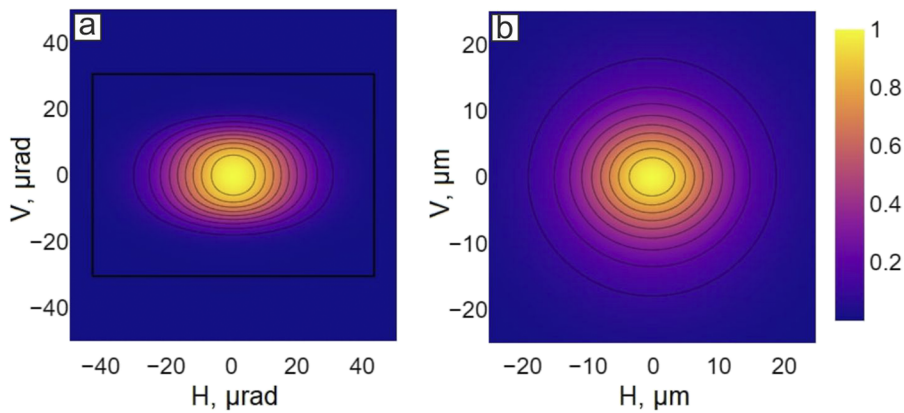


**FIG. 2.** (a) Angular characteristic (rms,  $\mu\text{rad}$ ) and (b) spatial profile (FWHM,  $\mu\text{m}$ ) of third harmonic in the undulator center. The flux densities are given in relative units. Black square marks the area transmitted through the primary aperture of  $86 \times 61 \mu\text{rad}^2$ .

modes with single/double and narrow/wide harmonics.<sup>5</sup> Principal scheme of the SCU operation is illustrated in Fig. 1.

The basic operational modes are single-line ones with bandwidths of  $10^{-2}$  and  $5 \times 10^{-2}$ . The double-line regimes could be implemented on request.

The characteristics of the “SKIF” facility (Table I) were used for simulations as an example of a low-emittance storage ring.<sup>6</sup>

Given the results of calculations, we settled on the following parameters of ID: period of magnetic field is 13.5 mm, the number

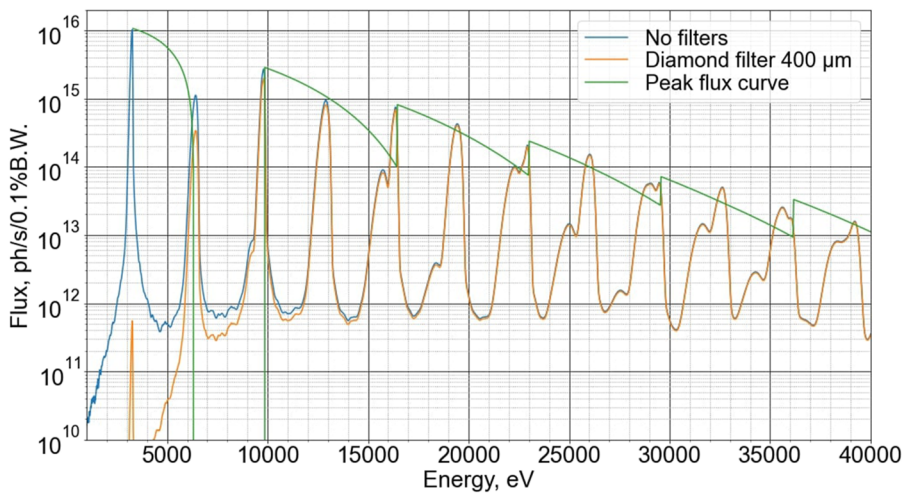


**FIG. 3.** The spectral flux density through an aperture of  $86 \times 61 \mu\text{rad}^2$  and peak flux curve without diamond filters. The SCU operates in a narrow single-line mode.

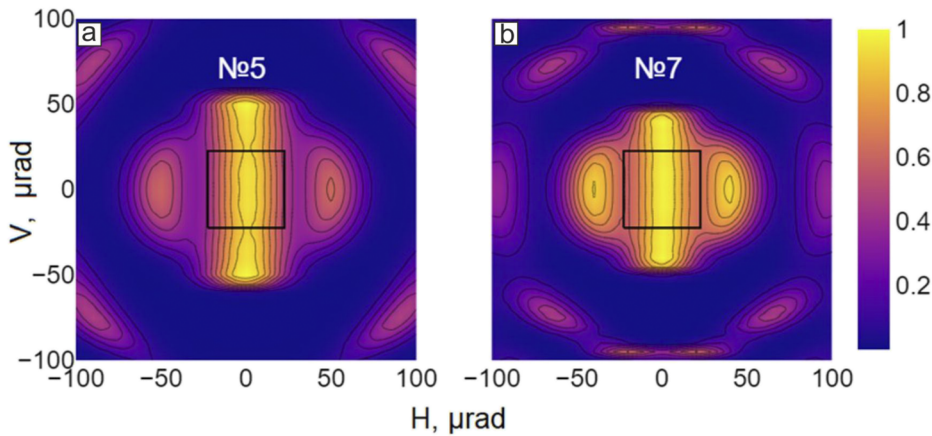


**FIG. 4.** Divergence of radiation in optimal modes for harmonics No. 5 (a) and No. 7 (b). Flux densities are given in relative units. Black square marks the area transmitted through the aperture of  $45 \times 45 \mu\text{rad}^2$ .

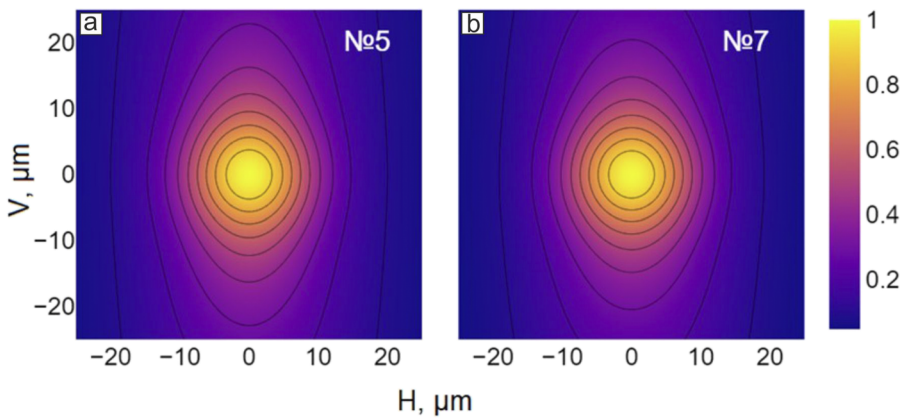


**FIG. 5.** Spatial profiles of harmonics in a center of the undulator in the mode of widened harmonics (FWHM,  $\mu\text{m}$ ) (a) No. 5 [ $17.5 \text{ (h)} \times 24.2 \text{ (v)}$ ] and (b) No. 7 [ $17.5 \text{ (h)} \times 22.5 \text{ (v)}$ ].

of periods in section is 140 (the sections are identical), the number of segments is 10 (the number of periods in each segment is 14), the field is 1.08 T, and full power of radiation from ID is about 10 kW. The highest field corresponds to the deflection parameter,  $K = 1.36$ ,

the energy of the fundamental harmonic is 3.3 keV. Phase error was taken as  $3^\circ$ .

Angular and spatial characteristics of harmonics in the narrow single-line mode of the SCU are presented for the main third

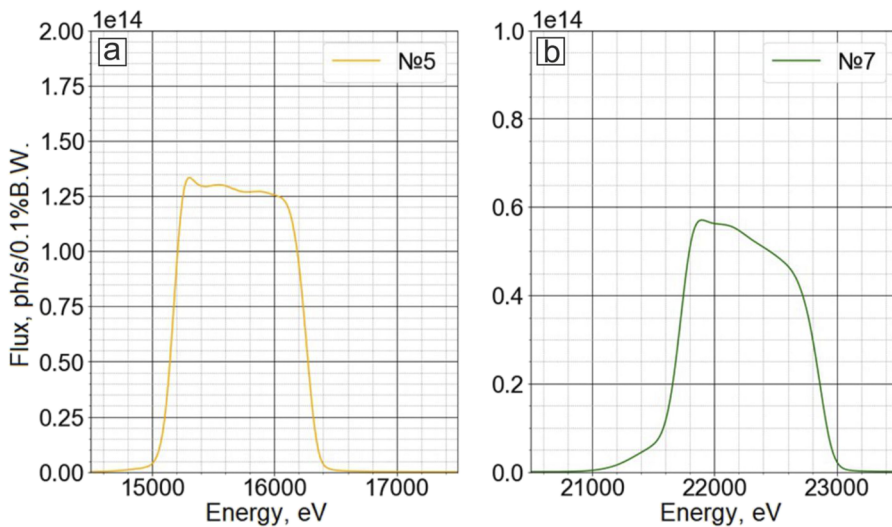


**FIG. 6.** The spectral flux density through an aperture of  $45 \times 45 \mu\text{rad}^2$  with diamond filters. The SCU operates in wide single-line mode. Harmonics No. 5 (a) and No. 7 (b).

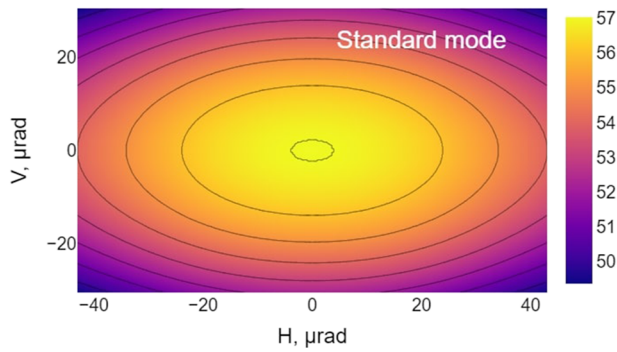


FIG. 7. Spatial distribution of power of radiation coming off the front-end in narrow single-line mode, in  $\text{mW}/\mu\text{rad}^2$ .

undulator harmonic in Fig. 2. Angular characteristics of harmonics (rms,  $\mu\text{rad}$ ) are No. 3 ( $14.3 \times 10.2$ ), No. 5 ( $13.6 \times 10.2$ ), No. 7 ( $13.2 \times 10.2$ ), and No. 9 ( $12.6 \times 10.5$ ). Calculations were made by SPECTRA 11 code.<sup>7</sup>

The value of angular aperture ( $86 \times 61 \mu\text{rad}^2$ ) corresponds to  $6\sigma_x \times 6\sigma_y$  of the third harmonic divergence (the first operational harmonic of the SCU). The resulting envelope of the photon flux spectral density through the above-mentioned primary angular aperture in the narrow single-line mode is given in Fig. 3. By varying the currents in SCU's coils, one can achieve the suitable energy in a range of 10–30 keV. It should be noted that the photon flux of the fundamental harmonic is out of range but leads to heat loads for consequent optics. In order to suppress extra heat loads we use diamond filters with the total thickness of 400  $\mu\text{m}$ . The spectral flux density through an aperture of  $86 \times 61 \mu\text{rad}^2$  is presented in Fig. 3.

Angular and spatial characteristics of harmonics in the wide single-line mode of the SCU are presented in Figs. 4 and 5, respectively. Note that the SCU is optimized separately for the fifth and seventh wide single-line mode harmonics in order to achieve an optimal bandwidth of  $5 \times 10^{-2}$  and spectral uniformity for realizing the Laue diffraction technique in the energy range of 15–25 keV as well as for QXAFS in a broader range. The angular aperture of  $45 \times 45 \mu\text{rad}^2$  (rectangular in Fig. 4) was selected due to the halo attenuation and transmission of a relatively homogeneous central part of widened harmonics.

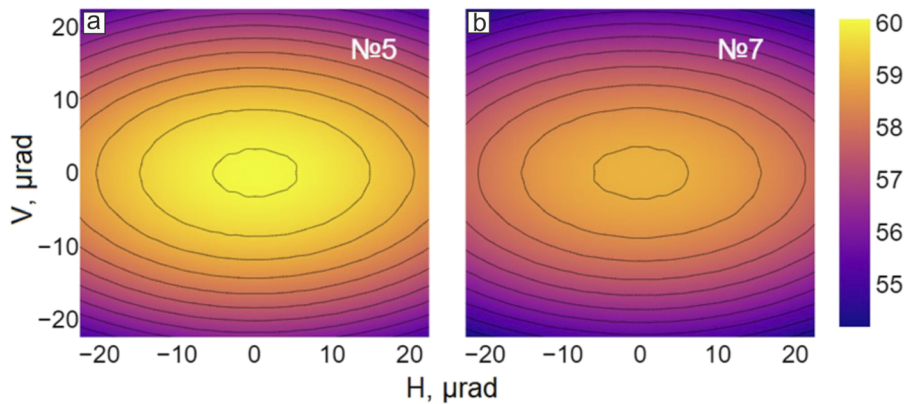


FIG. 8. Spatial distribution of power of radiation coming off the front-end in the mode of widened harmonics No. 5 (a) and No. 7 (b), in  $\text{mW}/\mu\text{rad}^2$ .

The spectral flux density through an aperture of  $45 \times 45 \mu\text{rad}^2$  is presented in Fig. 6.

The total power of radiation coming through the aperture of  $86 \times 61 \mu\text{rad}^2$  is 525 W. The diamond filters absorb 239 W, therefore, the beam power coming off the front-end is 286 W. The power density,  $\text{mW}/\mu\text{rad}^2$ , is given in Fig. 7.

The power coming through the aperture of  $45 \times 45 \mu\text{rad}^2$  in the optimal modes for the widened harmonics Nos. 5 and 7 is 211 and 208 W, respectively. The diamond filters absorb 87 and 86 W, therefore, the remaining power coming off the front-end is 124 and 122 W, respectively. The corresponding power density,  $\text{mW}/\mu\text{rad}^2$ , is plotted in Fig. 8.

For further calculations of thermal loads on the major beamline optics, the spatial distribution of the undulator radiation power in the narrow single-line mode was used, as a most exposed one to the heat load than the others.

#### IV. OPTICS: GENERAL SCHEME

The principle optical scheme of the “Materia” beamline is presented in Fig. 9. The beamline will operate as a “materials science microscope” with focusing and/or collimating modes ranging from 1 mm down to 100 nm. To achieve different focused (or collimated) beam spot sizes, the following optics systems are used separately or in combination: transfocator [based on beryllium compound refractive lenses (CRLs)], CRLs, and KB mirrors of final focus. The required spectral bands are achieved using either DMM or QCM (working in combination with DMM).

The following operation modes of the focusing optics are suggested:

- Optics taken away from the beam (no focusing);
- Beam collimation with transfocator;
- Focusing 1:1 with transfocator (with a possibility of operation in converging beams);
- Focusing 25:1 with CRLs (without collimation);
- Focusing with CRLs (with collimation by transfocator);
- Focusing 100:1 with KB mirrors (without collimation, CRLs taken away from the beam);
- Focusing with KB mirrors (with collimation by transfocator, CRLs taken away from the beam).

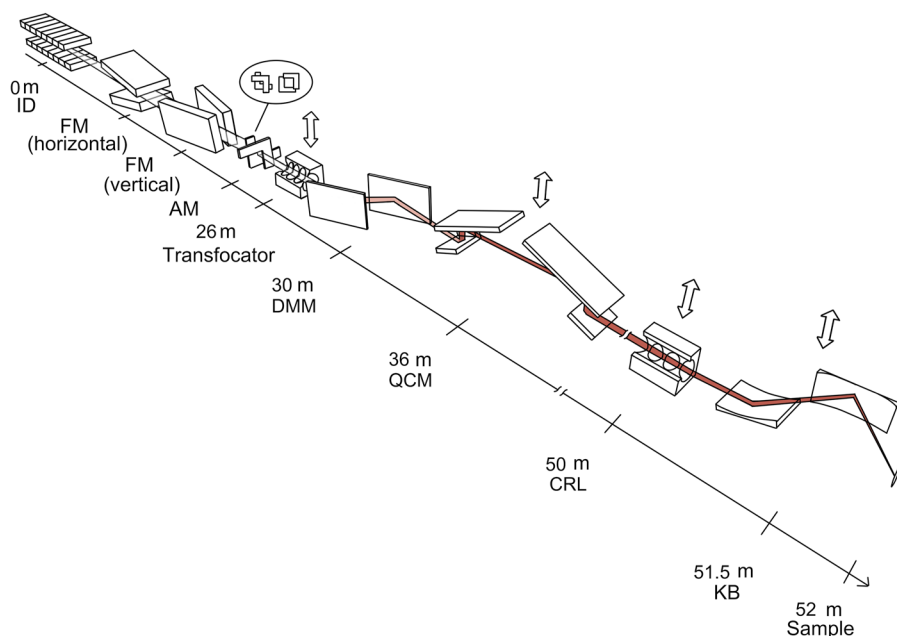


**FIG. 9.** General x-ray optical scheme of the “Materia” beamline. The figure indicates approximate distances from the radiation source to the beamline optics. (ID) insertion device; (FM) fixed horizontal or vertical masks; (AM) adjustable mask; Transfocator, a set of compound refracting lenses; (DMM) double multilayer monochromator; (QCM) quadruple crystal monochromator; (CRL) a set of compound refracting lenses of final focus; (KB) mirrors, Kirkpatrick-Baez mirrors of final focus.

In each of the listed modes, the primary monochromatization of radiation ( $10^{-2}$  or  $5 \times 10^{-2}$ ) is carried out by DMM. QCM is inserted into the beam path when/if needed—to obtain a more narrow spectral bandwidth.

It is assumed that the “Materia” beamline will be windowless from the radiation source to the experimental hutche operating under ultra-high vacuum conditions ( $10^{-9}$ – $10^{-8}$  mbar). The only beam attenuators and/or calibration filters (diamond and various metal foils) will be present in the beam path. A thin diamond window will be located to extract the beam into the atmosphere at the entrance of the experimental hutche at a distance of 41–42 m from the radiation source. The optics of the final focus will also be in evacuated (or vacuum-tight) volumes.

To achieve a maximum beamline optics stability, the major optical components (DMM and attenuators) will be always kept under a constant beam irradiation for the thermal equilibrium over the corresponding beamline’s operation time considered. The beam

position will be controlled by a number of monitors located both in the front-end and in the hutches. The remotely driven safety beam shutter will be located at the end of the optics hutche downstream of DMM and QCM.

### A. Transfocator

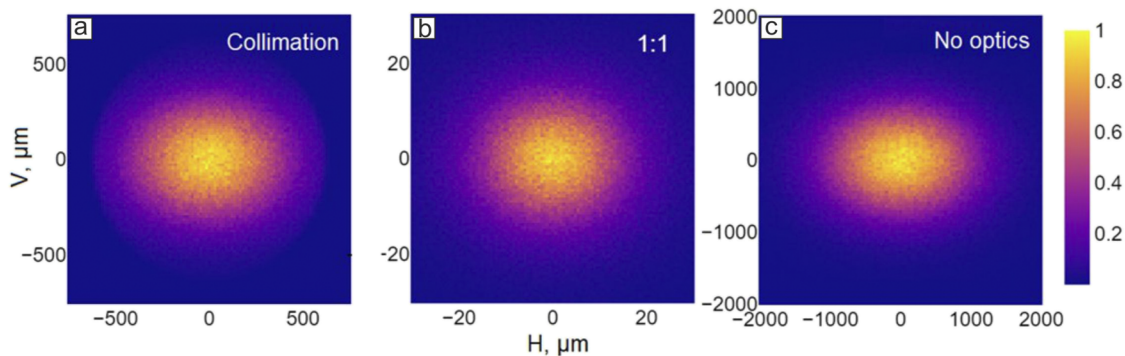
The transfocator is located in the optics hutche after the radiation-protection wall (first interface at 26 m from the radiation source). The transfocator will be used for beam collimation or for focusing in 1:1 ratio. The optimal radius of curvature of lenses,  $R$ , is defined by the request of keeping the highest radiation flux possible and minimization of the number of lenses in the transfocator device when working at different undulator harmonics. Thus, the radius of curvature is chosen to be  $R = 500 \mu\text{m}$  for all lenses.<sup>8</sup> In the future, with the development of manufacturing technology the diamond lenses will be considered as an alternative to Beryllium.

**TABLE II.** Beam parameters for collimating mode.

Photon energy, keV (harmonic’s number)	Number of CRLs	Focal length (m)	Focused beam spot size, FWHM ( $\mu\text{m}$ )		Photon flux (ph/s)		
			H	V	Si/Be	Cr/Be	W/Be
9.9 (3)	3	24.0	690	490	$7.09 \times 10^{15}$	...	...
16.4 (5)	8	24.7	660	510	$3.40 \times 10^{15}$	$2.57 \times 10^{15}$	$2.36 \times 10^{15}$
23 (7)	14	25.9	710	580	...	$8.57 \times 10^{14}$	$6.29 \times 10^{14}$
29.6 (9)	25	25.7	600	520	...	$2.46 \times 10^{14}$	
16.4 (5w)	7	24.0	1086	1086	...	...	$1.18 \times 10^{15}$
23 (7w)	14	25.3	1112	1113	...	...	$2.13 \times 10^{14}$

**TABLE III.** Beam parameters for 1:1 focusing mode.

Photon energy (keV) (harmonic's number)	Number of CRLs	Image distance (m)	Focused beam spot size, FWHM ( $\mu\text{m}$ )		Photon flux (ph/s)		
			H	V	Si/Be	Cr/Be	W/Be
9.9 (3)	5	29.9	27	21	$6.57 \times 10^{15}$	...	...
16.4 (5)	14	28.6	33	27	$3.10 \times 10^{15}$	$2.35 \times 10^{15}$	$2.15 \times 10^{15}$
23 (7)	28	27.0	29	26	...	$7.38 \times 10^{14}$	$5.41 \times 10^{14}$
29.6 (9)	47	26.6	23	23	...	$2.03 \times 10^{14}$	...
16.4 (5w)	13	28.9	35	45	...	...	$1.04 \times 10^{15}$
23 (7w)	28	26.5	29	35	...	...	$1.72 \times 10^{14}$

**FIG. 10.** Beam spot shapes at the sample plane (52 m from the source) for the third undulator harmonic. (a) Collimation mode, (b) 1:1 focusing, (c) no optics.

The results of simulations for the transfocator (number of lenses, focal distance, beam spot size, and flux on sample) in the beam collimation and focusing modes are presented in Tables II and III, respectively. The simulations were performed using the *Shadow 3* software package<sup>9</sup> for the magnetic field that corresponds to the maximum of intensity of undulator harmonics. The double reflection from the DMM as well as absorption coefficients with additional filters (described in the “DMM + QCM” section below) was taken into account. The Si/Be and Cr/Be multilayer mirrors are selected for the pre-monochromatization in a standard SCU operating mode and the W/Be one for the wide single-line mode. Note that the W/Be mirrors can also be used in a standard mode of the SCU operation. The calculation results indicate both cases of use of the W/Be mirrors, with a letter “w” marking widened harmonics.

Examples of the source image for collimation and 1:1 focusing modes of transfocator are presented in Fig. 10. The image of the source without a transfocator is also shown. A ray-tracing simulations were carried out for the third harmonic of the SCU.

## B. Monochromators

At the “Materia” beamline, it is planned to install both the horizontally deflecting double-multilayer monochromator (DMM) and the vertically deflecting quadruple crystal monochromator (QCM). They can work either in combination or individually. The QCM will provide the final beam monochromatization,  $\Delta E/E$ , of  $1.3 \times 10^{-4}$  with Si (111) crystals where requested.

### 1. Double-multilayer monochromator (DMM)

A double-mirror multilayer monochromator consists of a pair of flat mirrors arranged vertically, i.e., the reflection plane of the DMM is horizontal. The DMM is intended for monochromatization of the SR beam with  $\Delta E/E$  of about  $10^{-2}$  and  $5 \times 10^{-2}$  or (when paired with QCM) for primary monochromatization and reducing the thermal load on the first QCM crystal.

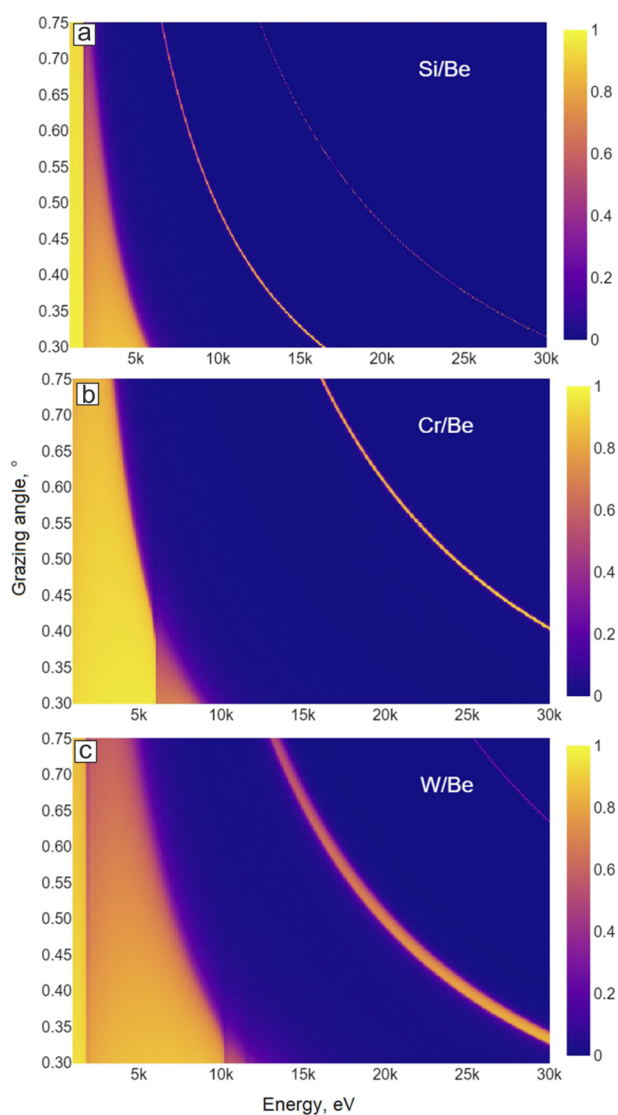
The mirror coating will consist of three strips 5 mm wide: Si/Be, Cr/Be and W/Be. The Si/Be and Cr/Be pairs with  $\Delta E/E = 10^{-2}$  cover the main energy range of 10–30 keV, whereas the W/Be pair with  $\Delta E/E = 4.6 \times 10^{-2}$  is designed to operate in the extended fifth or seventh undulator harmonics mode. Coating parameters are presented in Table IV, reflectivity of multilayers—in Fig. 11. Calculations were performed taking into account the substrate roughness (rms) of 3 Å and the interlayer roughness (rms) of 3 Å using the multifitting code<sup>10</sup> and the XOP code.<sup>11</sup> Grazing angles range from  $0.3^\circ$  (fifth harmonic of the SCU, Si/Be mirrors) to  $0.75^\circ$  (fifth harmonic of the SCU, Cr/Be mirrors). The optimal length of the mirror to capture the whole beam is about 300 mm.

For the selected range of grazing angles of incidence,  $0.3^\circ$ – $0.75^\circ$ , we considered the scheme of translating the mirrors and possible variant of the DMM construction as shown in Fig. 12. The full range of longitudinal translation of the second mirror required against the fixed position of the first mirror with an offset of  $H_{\text{offset}} = 15$  mm is L, from 573 to 1432 mm, i.e., 859 mm. No horizontal adjustment of mirrors is required [in direction D, Fig. 12(a)] since shift of the second mirror will be less than 1  $\mu\text{m}$ . The change

**TABLE IV.** Parameters of DMM multilayer coatings.  $N$  is the number of layers,  $\gamma$  is the ratio of the thickness of the even sublayer to the thickness of the period of the structure.

Strip, No.	Coating	Period ( $\text{\AA}$ )	$N$	$\gamma$	Energy range (keV)	$\Delta E/E$	Grazing angles (deg)
1	Si/Be	76.6	300	0.33	9–16	$10^{-2}$	0.3–0.5
2	Cr/Be	30	300	0.33	16–30	$10^{-2}$	0.4–0.75
3	W/Be	38	150	0.40	16–25	$4.6 \times 10^{-2}$	0.4–0.6

of the working strips of mirrors will be simply made by their vertical translation (along coordinate  $Y$ ) across the beam by 12–15 mm. Note that an offset of 15 mm makes it easy to install Bremsstrahlung radiation shielding in the optics hutch.

**FIG. 11.** Multilayer structures reflectivity: (a) Si/Be, (b) Cr/Be, (c) W/Be.

The novelty of our concept is the use of vacuum chambers of relatively small size and the removal of all critical, precision movements from the vacuum to the outside into the atmosphere [Fig. 12(b)]. The device uses three, with a diameter of about 400 mm, short vacuum chambers. The first (on the left along the incident beam) and the last [No. 3 in Fig. 12(b)] chambers remain stationary in the direction of the optical axis of the device, and the second chamber moves widely. The multilayer mirrors are placed in the first and second chambers. The first chamber is mounted on a motion system that provides all necessary adjustments and movements (pitch, vertical, and horizontal translations). Vertical movement is due not only to the precise adjustment of the monochromator to the incoming beam but also allows us to quickly change the type of working multilayers' strip. The movement system of the second chamber, in addition to those noted above, includes a long-range, longitudinal, linear translation stage of  $\sim 1$ -m travel for scanning the energy. To ensure the required kinematics of the device, the central chamber is connected to the fixed chambers by means of a welded bellows providing a range of movements of more than four times relative to the compressed state. The whole device is mounted on a massive, stable granite table. The total length (from flange to flange) of entire system is estimated to be about 3 m.

The heat released into the mirrors is one of the crucial issues in the design of DMM. The absorption of a heat leads to the thus-induced shape and slope errors causing undesirable focusing or defocusing effects.<sup>12</sup> For this reason, a thorough numerical simulation of temperature distribution and corresponding deformations of the mirror was carried out. The spatial distribution of incident power density, shown in Fig. 13, was calculated by SPECTRA 11 software. It was assumed that all power was absorbed by the mirror, and the heating source was surficial. A rather severe operation mode with grazing angle of  $0.75^\circ$  and an absorbed power of 287 W was chosen for simulations. The thermal analysis for the stationary case was carried out using the ANSYS 2020R2 simulation software (Fluent module).

The geometry, which was used for calculations and boundary conditions, is shown in Fig. 14. The “smart cut” design was chosen for the mirror geometry following the recommendation of previous studies.<sup>12,13</sup> This means that the mirror had small notches along the cooled sides. The effect of these notches is to reduce the slope error. The cooling is made by copper heat exchangers, attached to both sides of the mirror. The temperature of water in the heat exchanger was defined to be 295 K and mass flow rate of water 5 l/h.<sup>12,14</sup> The conditions for radiative heat exchange with the environment were set for the side and bottom planes of the mirror for  $T_0 = 295$  K and  $\varepsilon = 1$ . The temperature dependence of silicon thermo-mechanical

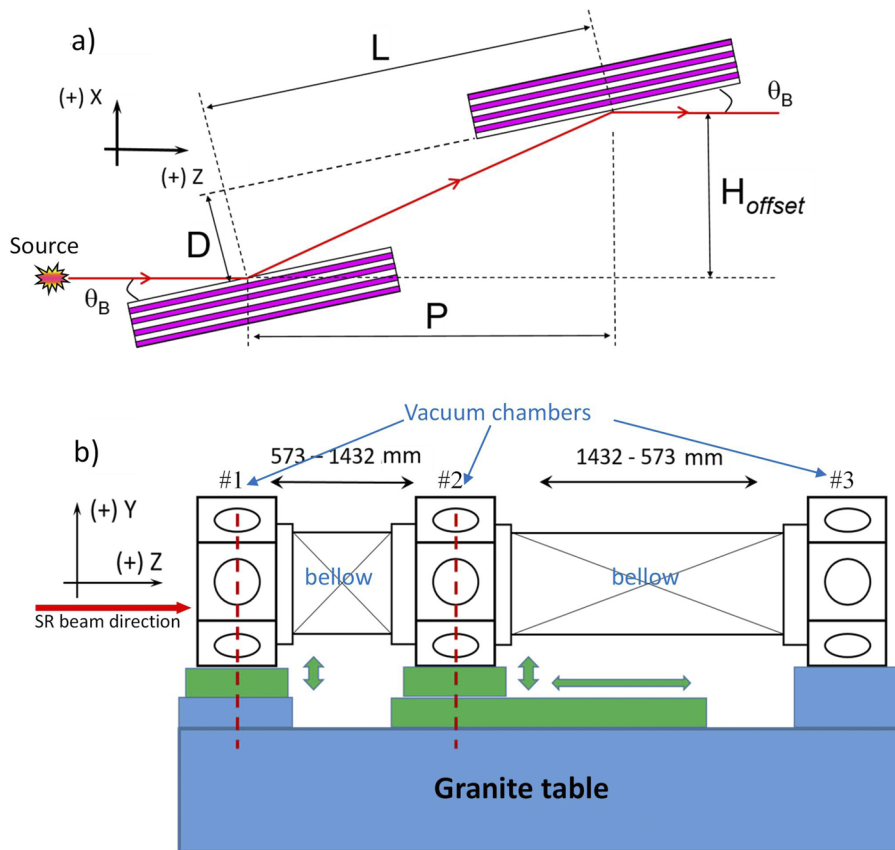


**FIG. 12.** (a) Multilayers geometry:  $L$  is a distance between centers of mirrors along the reflecting planes of mirrors,  $D$  is a spacing between the reflecting planes of mirrors,  $P$  is a distance between the centers of mirrors along the beam source direction. (b) Schematics of DMM construction with vacuum volumes bound with bellow knots on one common vibration-resistant plate/platform. The red dot lines mark the axes of mirrors' rotations; the ranges of compression-expansion of bellows, outside translation linear stages (two vertical and one long-range longitudinal stages) are also shown (in green).

properties was taken into account.<sup>15</sup> The dependences of the linear thermal expansion coefficient of silicon were used<sup>16,17</sup> for ANSYS 2020R2 calculations of the stress-strain state of the mirror during heating.

Figure 15 shows the distributions of temperatures and displacements simulated. It concludes that the main temperature change of a mirror surface occurs in the region where the heat flux is actually applied.

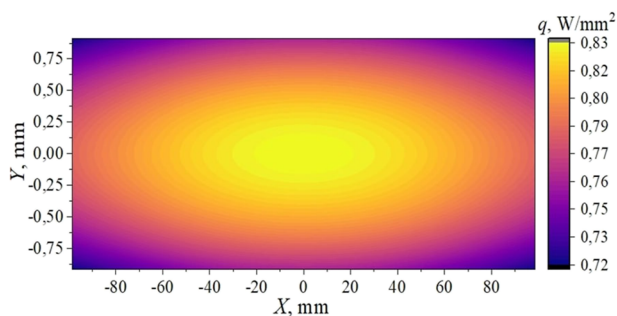


**FIG. 13.** Absorbed power density.

Figure 16 shows local temperature, displacement, and angular strain profiles in the  $Y$ - $Z$  and  $X$ - $Z$  planes. Consequently, the permissible parameters of angular displacements, in accordance with the recommendations of the article,<sup>12</sup> can be satisfied by cooling the mirror with just a water as a coolant.

Resulting flux densities of a beam passed through the DMM are given in Fig. 17 for the standard SCU mode and in Fig. 18 for the wide fifth and seventh harmonics modes. It has been established that when the DMM is used in the region of high harmonics, the transmitted radiation spectrum is contaminated with parasitic soft x-rays due to total reflection. Therefore, additional filters are suggested. The materials and thicknesses of these filters are shown in the figure legends as well as the harmonic coefficients  $Ch_n$ , defined as  $Ch_n = \sqrt{\sum_{i \neq n} F_i^2} / F_n \times 100\%$ , where  $F$  is a harmonic's peak spectral flux density,  $i$  is a harmonic number,  $n$  is a number of the operational harmonic.

One more advantage of using DMM as the major optical element of the beamline in spectroscopic (first of all, XAFS) studies should be noted. As can be seen from Fig. 18, multilayer mirrors effectively suppress higher order harmonics of the SCU, which excludes the necessity for any additional harmonic rejection mirror in the beamline.

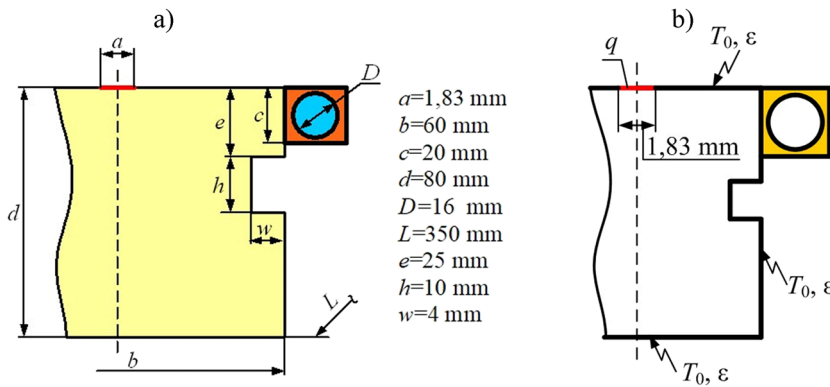


FIG. 14. Mirror geometry (a) and boundary conditions for thermal analysis (b).

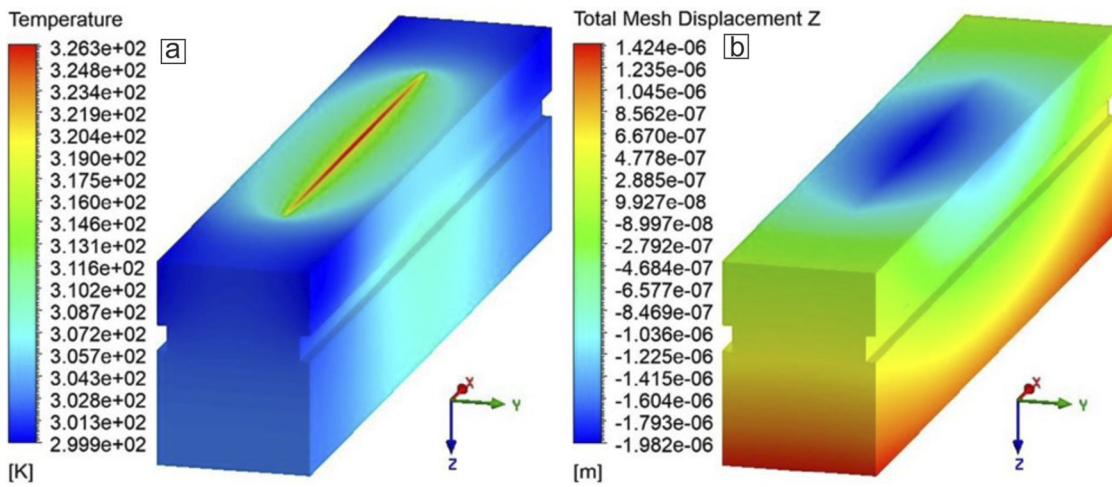


FIG. 15. Results of thermal and deformation calculations: (a) distribution of temperature, (b) material displacement.

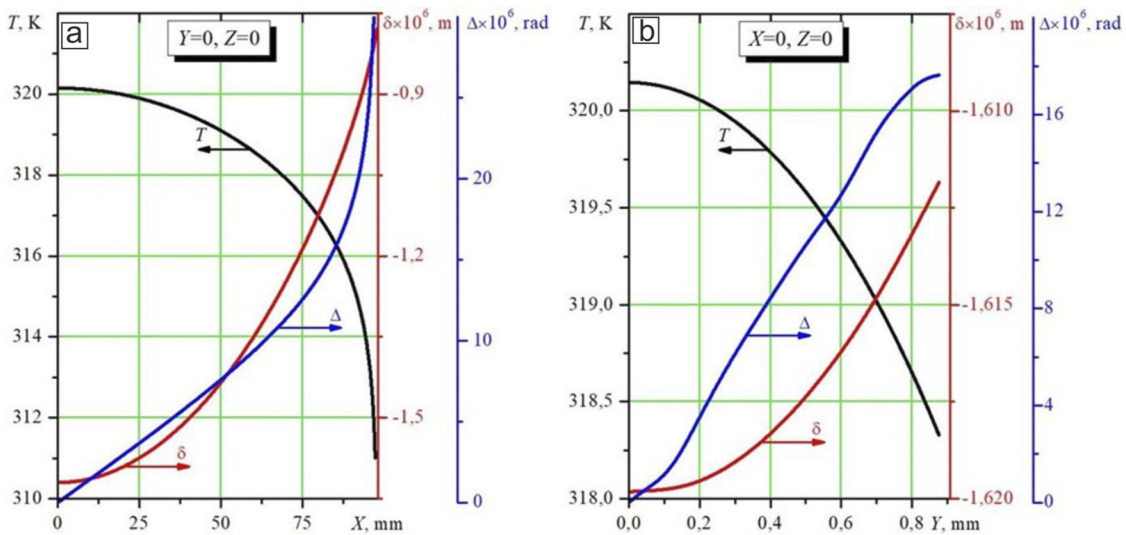
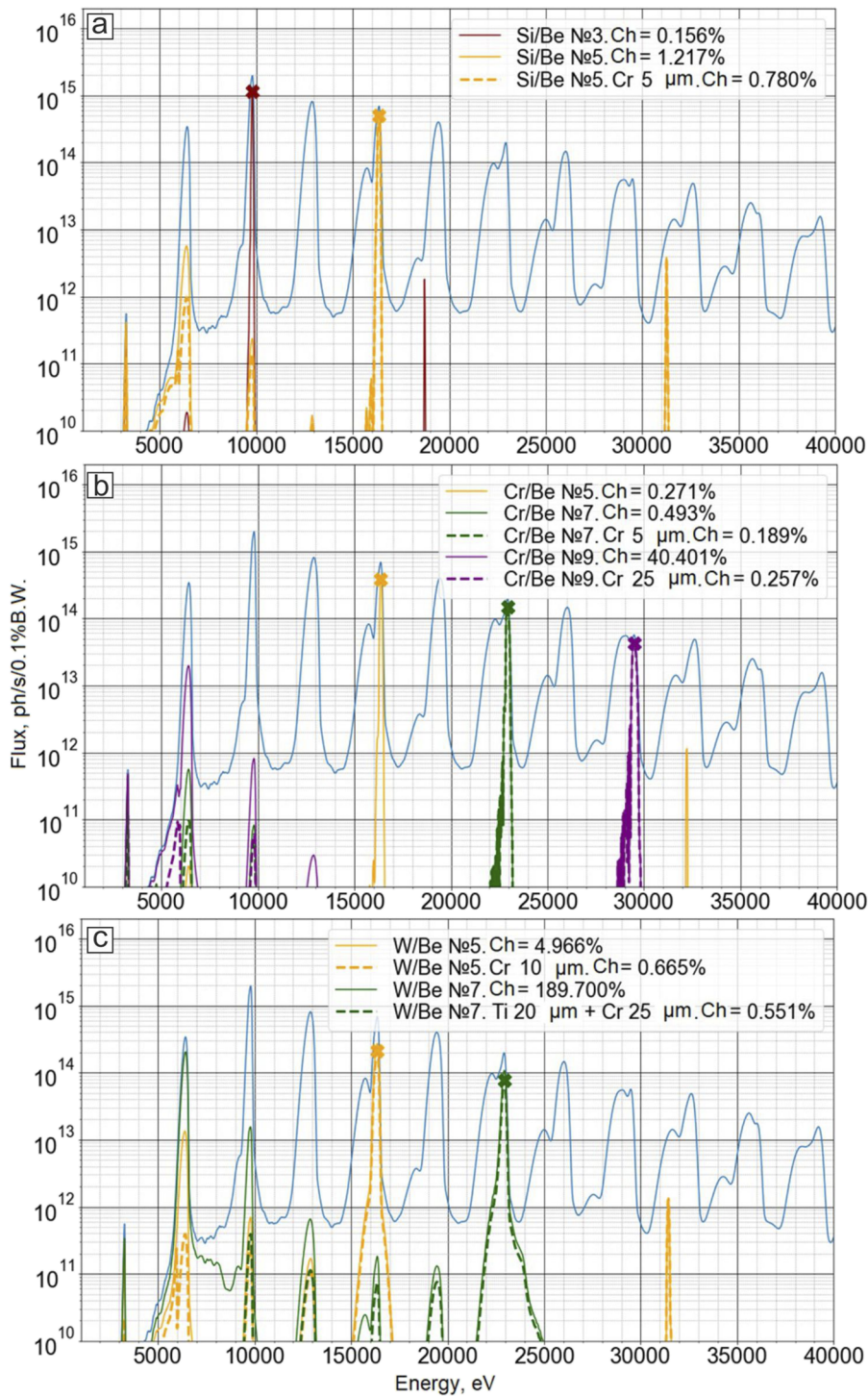


FIG. 16. Profiles of temperature, displacement, and slope:  $T$ , temperature (K),  $\delta$ , displacement (m),  $\Delta$ , slope (rad): (a) Y-Z plane, (b) X-Z plane.



**FIG. 17.** Spectral flux densities after DMM in the standard mode of the SCU for Si/Be (a), Cr/Be (b), and W/Be (c) strips.

## 2. Quadruple crystal monochromator (QCM)

The QCM consists of a mirror-symmetrical pair of channel-cut Si (111) crystals and is designed for final monochromatization (with  $\Delta E/E \sim 10^{-4}$ ). The reflection plane is chosen to be vertical, i.e., orthogonal to the reflection plane of the DMM in order to

decouple the two rotary systems of DMM and QCM from each other.

The main advantage of using the QCM is the preservation of beam position at the sample plane while operating several experimental methods at the same energy or when the photon energy is being scanned, as well as during insertions/removals of the QCM

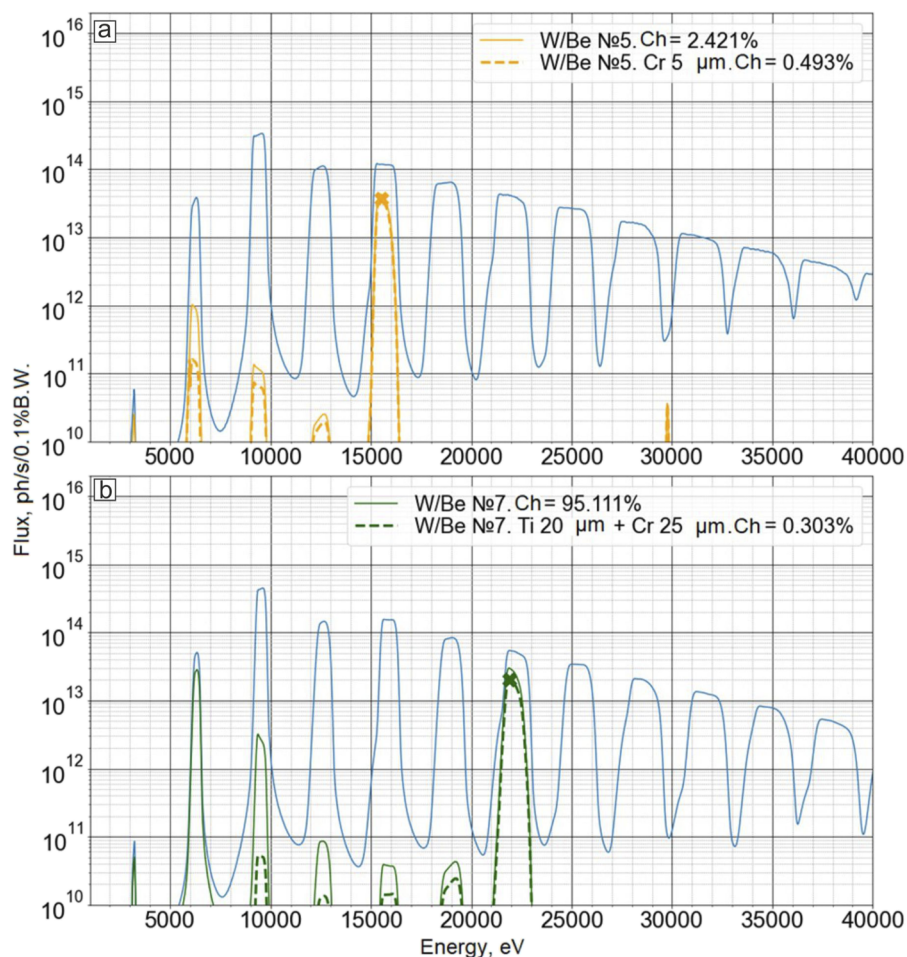


**FIG. 18.** Spectral flux densities after DMM in the wide fifth and seventh harmonics modes of the SCU: (a) optimized for fifth harmonic, (b) optimized for seventh harmonic.

from the beam path and when the QCM is being tuned to another undulator harmonic or inside the broadened harmonic during the same experiment. An additional advantage of using the QCM is the ability to relatively easy implement the fast energy scanning, which is essential for performing QXAFS with XANES data acquisition rates up to at least 1 kHz. The combination of the wide-harmonic mode of the SCU and the “DMM + QCM” system will allow a fast energy scans during experiments, which are critical for QXAFS and Laue diffraction techniques.

We should note that the first crystal of QCM undergoes the highest thermal load in the mode of passing the third harmonic (strip Si/Be of DMM) with a total radiation power of  $\sim 14$  W, which is rather high. The Bragg angle corresponding to the maximum of the third undulator harmonic is  $11.63^\circ$  equivalent to the photon energy of 9.9 keV. The calculated power density distribution for such a case is presented in Fig. 19.

To simplify a task, the thermal calculations and calculations of deformations of the first crystal of QCM were performed with the help of numerical models built for DMM. The principal question that we were looking the answer to was whether there is an alternative for liquid nitrogen cooling with such high thermal loads (Figs. 20 and 21).

As can be seen from the resulting profiles (induced surface displacements and angular slopes) presented in Fig. 21, the largest slopes are observed at the periphery of the beam and are about  $0.3\text{--}0.4 \mu\text{rad}$ . Thus, we can conclude that the use of liquid nitrogen as a coolant is a reasonable choice because this is much less than the Darwin’s width of the Si(111) crystal rocking curve at this specific energy/Bragg angle.

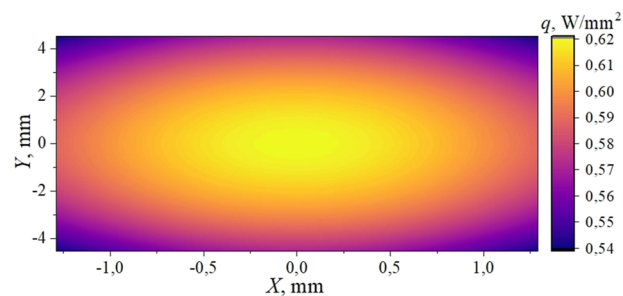


**FIG. 19.** Absorbed power density for QCM at grazing angle of  $11.63^\circ$ , and a total absorbed power of 14 W.

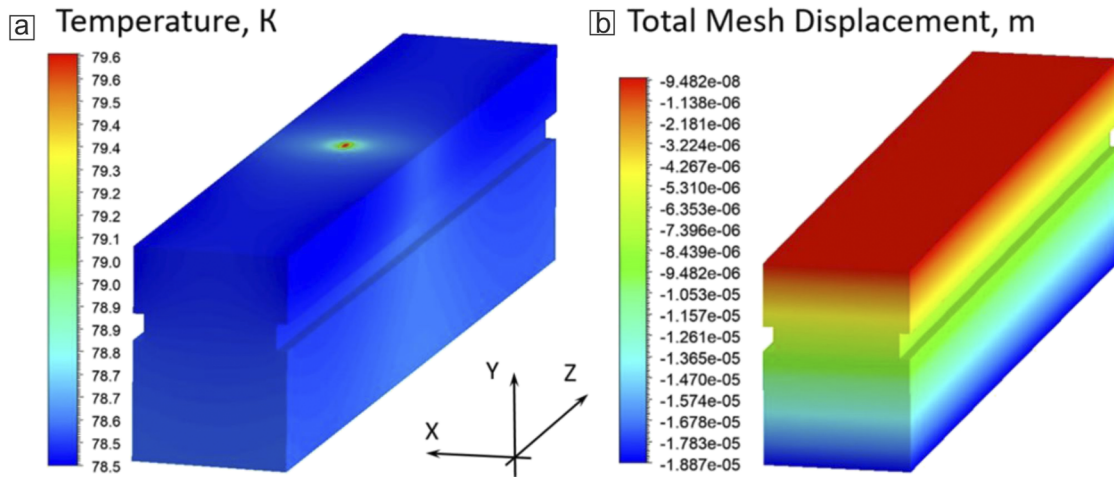


FIG. 20. Volume steady distribution of temperature (a) and linear displacements (b) of the first crystal with the Bragg angle of  $11.63^\circ$ . Case of liquid nitrogen cooling.

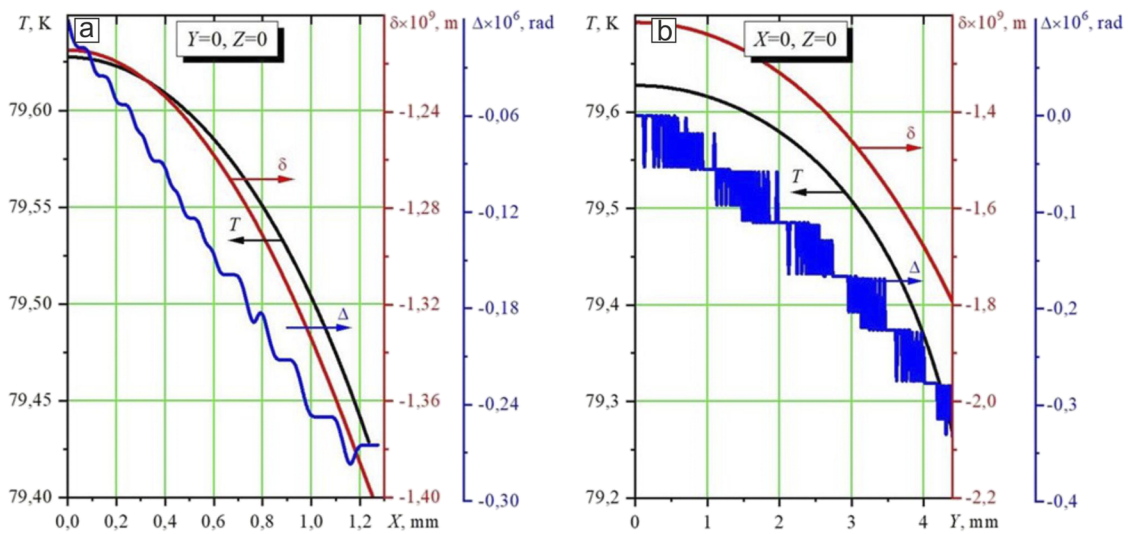


FIG. 21. Profiles of temperature, displacement, and slope:  $T$ , temperature (K),  $\delta$ , displacement (m),  $\Delta$ , slope (rad): (a) Y-Z plane, (b) X-Z plane.

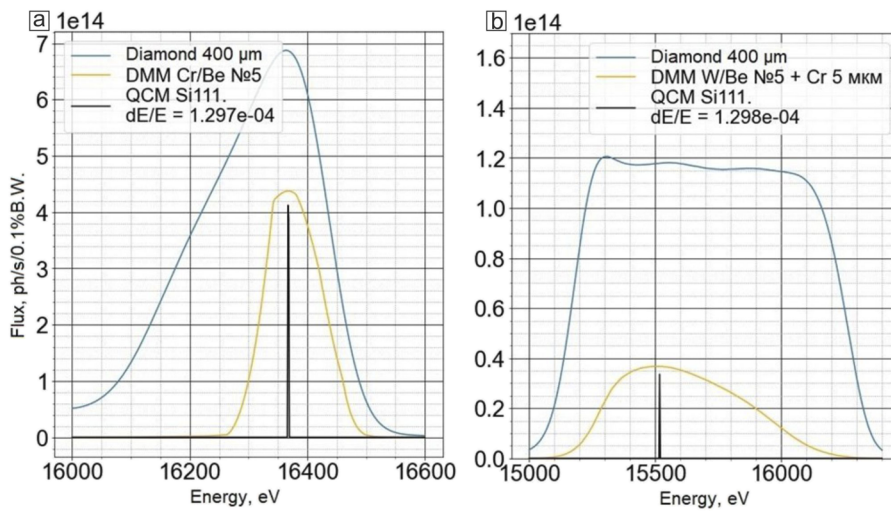


FIG. 22. Spectral flux densities after DMM and QCM in the standard (a) and the wide fifth harmonic (b) modes of the SCU.

Finally, examples of resulting flux densities (fifth harmonic) passed through both the DMM and QCM are given in Fig. 22: on the left—for the standard SCU mode, on the right—for the wide line mode.

### 3. Final focus optics: CRLs

Among elements of optics of final focus is a set of compound refractive lenses (CRLs), the first interface of which is located at a distance of ~50 m from the center of the SCU. CRLs of final focus are

intended for the 25:1 focusing ratio. The results of calculations are presented in Table V. An example of the source image obtained at a distance of 52 m from the source is given in Fig. 23 (left). As in case with transfocator, we looked at using identical lenses. The lens radius  $R = 200 \mu\text{m}$  (at parabola's apex) was selected so that the geometric aperture of CRL ( $880 \mu\text{m}$ ) completely passes the beam collimated by the transfocator.

To increase the radiation flux on the sample, we also considered the option in which CRLs of final focus are used together with transfocator, the latter working in collimation mode. The results

TABLE V. Parameters of Be CRLs of final focus. Radius of curvature of lenses,  $R = 200 \mu\text{m}$ .

Energy of photons (keV) (harmonic's number)	Number lenses	Distance from first interface to waist (mm)	Size of radiation spot in focus (FWHM) ( $\mu\text{m}$ )		Number of photons per second after passing DMM (elemental composition of pairs of multilayered mirrors is indicated) and CRL		
			H ( $\mu\text{m}$ )	V ( $\mu\text{m}$ )	Si/Be	Cr/Be	W/Be
9.9 (3)	14	2090	1.64	1.4	$9.76 \times 10^{14}$	...	...
16.4 (5)	40	2038	1.74	1.62	$4.39 \times 10^{14}$	$3.32 \times 10^{14}$	$3.05 \times 10^{14}$
23 (7)	81	2011	1.48	1.66	...	$8.54 \times 10^{13}$	$6.26 \times 10^{13}$
29.6 (9)	138	2044	1.31	1.27	...	$1.69 \times 10^{13}$	...
16.4 (5w)	35	2170	1.84	2.24	...	...	$7.73 \times 10^{13}$
23 (7w)	72	2229	2.08	2.48	...	...	$1.11 \times 10^{13}$

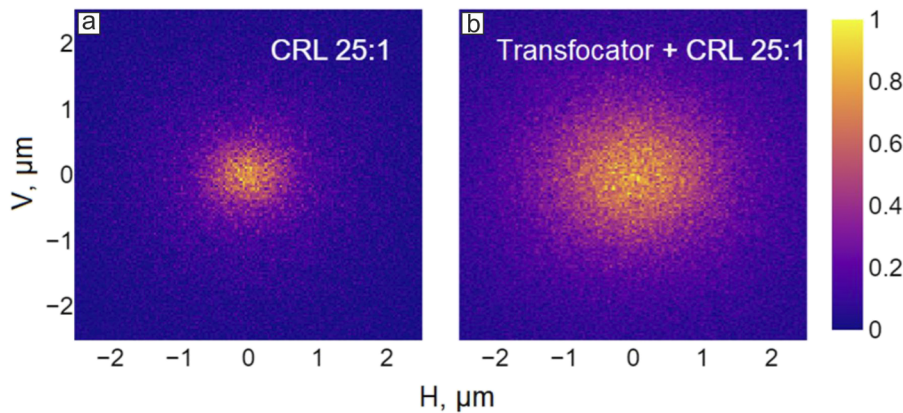


FIG. 23. Source images calculated for the third undulator harmonic at 52 m from the source with focusing by only lenses of final focus (a) and lenses of final focus together with the collimating transfocator (b). Intensity is given in relative units. The calculations were performed using the Shadow software and do not take into account possible coherence effects that can result in the appearance of diffraction-induced features in the beam.

TABLE VI. Parameters of final focus in the “transfocator + CRL” configuration.

Energy of photons (keV) (harmonic's number)	Beam spot size at focus (FWHM) ( $\mu\text{m}$ )		Number of photons per second after passing zoom lens, DMM (elemental composition of pairs of multilayered mirrors is indicated) and CRL		
	H ( $\mu\text{m}$ )	V ( $\mu\text{m}$ )	Si/Be	Cr/Be	W/Be
9.9 (3)	2.65	2.1	$3.16 \times 10^{15}$	...	...
16.4 (5)	2.89	2.6	$1.38 \times 10^{15}$	$1.04 \times 10^{15}$	$9.56 \times 10^{14}$
23 (7)	2.38	2.14	...	$2.38 \times 10^{14}$	$1.74 \times 10^{14}$
29.6 (9)	2.06	2.06	...	$5.62 \times 10^{13}$	...
16.4 (5w)	2.88	3.92	...	...	$2.83 \times 10^{14}$
23 (7w)	2.88	3.52	...	...	$3.76 \times 10^{13}$

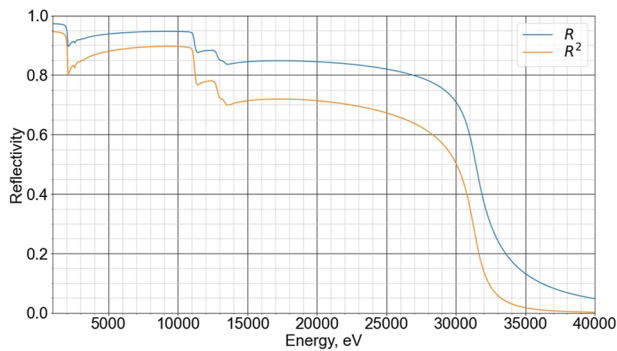


FIG. 24. Ir reflectivity with fixed grazing angle of 2.75 mrad.

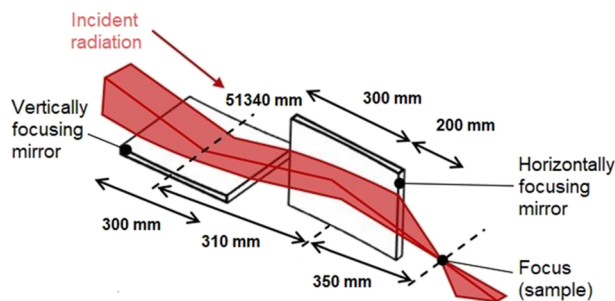


FIG. 25. Beam path with focusing by KB mirrors and geometric parameters of the system.

of calculations are summarized in Table VI. An example of the source image obtained at 52 m is given in Fig. 23 (right). In this case, the beam spot size on the sample increases up to  $2.5 \mu\text{m}$ , i.e., approximately by 1.6 times, and the flux increases by  $\sim 3$  times as we expected.

#### 4. Final focus optics: KB mirrors

Another element of final focus is Kirkpatrick-Baez mirrors' system. KB mirrors are used in the scheme where the first mirror focuses the beam vertically and the second one horizontally.

A coating of KB mirrors is iridium, Ir. The grazing angle for a range of energies up to 30 keV was chosen to be 2.75 mrad (criterion—no less than 50% of radiation is saved after double reflection). The Ir reflection coefficient as a function of energy at the fixed grazing angle of 2.75 mrad is shown in Fig. 24. The calculations were made assuming a roughness (rms) of 3 Å using the XOP software code.

For optimization of mirrors, we considered the following conditions: the distance from the edge of the second, last mirror to the focal plane (=sample) must be no less than 200 mm, the typical size of a beam spot on the sample must be about 100 nm, and the system of KB mirrors must catch all SR beam collimated by transfocator. The distance of 200 mm (free distance of 150–170 mm to set up the experiment) is selected so that it would be possible to accommodate a large user's equipment and installations. With the designed mirror length of 300 mm the geometric aperture of the system is  $\sim 825 \times 825 \mu\text{m}^2$ . In this geometry (Fig. 25), the center of the first mirror must be located at a distance of 51.34 m from the center of the SCU, the center of the second mirror at 51.65 m. Such a system of KB mirrors allows for the realization of the final focusing with the optical "lever arm" of 78:1 vertically and 148:1 horizontally, the meridional radii of curvature in the centers of mirrors are 474 and 253 m, respectively. In our calculations, we assumed that for focusing the SR beam with KB mirrors, the CRLs of final focus are taken out from the optical beam path.

An example of source image in the focal plane (at a distance of 52 m from ID) is given in Fig. 26, the results of calculations of KB mirrors using the Shadow 3 code are presented in Table VII. For understanding real beam parameters in the focus, we have introduced a randomly Shadow-generated mirror's profile with figure error (rms of deviation from a perfect mirror shape) of 1 nm, which can be readily reached by processing the surface.<sup>18</sup> The slope angular error corresponding to this mentioned figure error is about 70 nrad. It should be noted that the radiation power focused by the optical system can reach 3.2 W and the power density in the center of the beam spot is  $79 \mu\text{W}/\text{nm}^2$ .

To increase the flux on the sample, we also considered the scheme where KB mirrors are used together with the transfocator (in collimation mode). In this case, the beam size on the sample increases up to  $1.2 \mu\text{m}$ . The results of calculations of this operating mode are given in Table VIII. An example of the source image obtained at 52 m from the source is presented in Fig. 27.

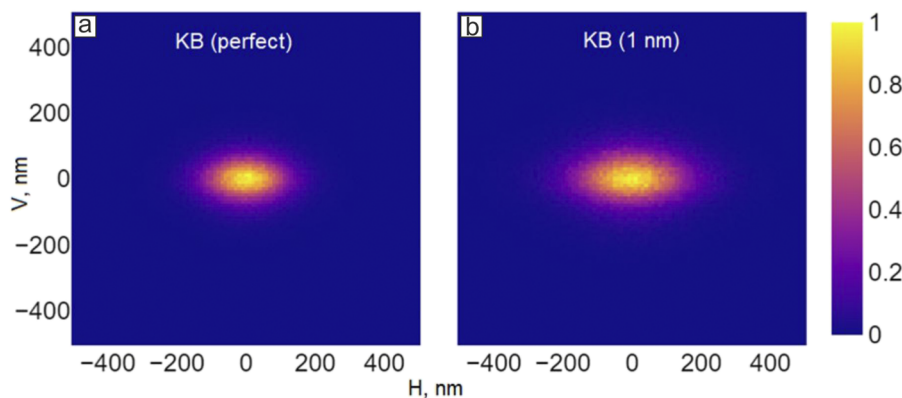


FIG. 26. Source image calculated for the third undulator harmonic at a distance of 52 m from the source with focusing by KB mirrors without (a) and with (b) the corresponding figure error (rms) of 1 nm. The size (FWHM, nm): 178 (h)  $\times$  99 (v) and 248 (h)  $\times$  109 (v), respectively. H, horizontal, V, vertical. Intensity is given in relative units. The calculations were performed using the Shadow software and do not take into account possible coherence effects that can result in the appearance of diffraction-induced features in the beam.

**TABLE VII.** Parameters of final focus for the system of KB mirrors. Here and after the sizes are given under the assumption of mirror's figure errors (rms) of 1 nm.

Energy of photons (keV) (harmonic's number)	Beam spot size in focus (FWHM) (nm)		Number of photons per second after passing DMM and KB mirrors (pairs of elements of multilayered mirrors are indicated)		
	H	V	Si/Be	Cr/Be	W/Be
9.9 (3)	248	109	$1.99 \times 10^{15}$	...	...
16.4 (5)	248	109	$7.97 \times 10^{14}$	$6.03 \times 10^{14}$	$5.54 \times 10^{14}$
23 (7)	257	109	...	$2.09 \times 10^{14}$	$1.53 \times 10^{14}$
29.6 (9)	257	129	...	$3.82 \times 10^{13}$	...
16.4 (5w)	337	109	...	...	$1.41 \times 10^{14}$
23 (7w)	317	109	...	...	$2.68 \times 10^{13}$

**TABLE VIII.** Calculations of the system "Transfocator + KB."

Energy of photons (keV) (harmonic's number)	Beam spot size in focus (FWHM) ( $\mu\text{m}$ )		Number of photons per second after passing DMM and KB mirrors (pairs of elements of multilayered mirrors are indicated)		
	H	V	Si/Be	Cr/Be	W/Be
9.9 (3)	1.27	1.27	$5.39 \times 10^{15}$	...	...
16.4 (5)	1.27	1.14	$2.07 \times 10^{15}$	$1.57 \times 10^{15}$	$1.44 \times 10^{15}$
23 (7)	1.11	0.98	...	$4.80 \times 10^{14}$	$3.52 \times 10^{14}$
29.6 (9)	1.19	1.23	...	$9.75 \times 10^{13}$	...
16.4 (5w)	1.18	1.29	...	...	$5.22 \times 10^{14}$
23 (7w)	1.27	1.27	...	...	$8.97 \times 10^{13}$

Note, the calculations given above are made in geometric approximation. The transverse coherence length for radiation with a wavelength  $\lambda$  at a distance R from the source with the rms size of  $\sigma_{x,y}$  is defined as<sup>19</sup>

$$t_c^{(t)} [m] = 28.21 \frac{\lambda [\text{\AA}] R [m]}{\sigma_{x,y} [m]}.$$

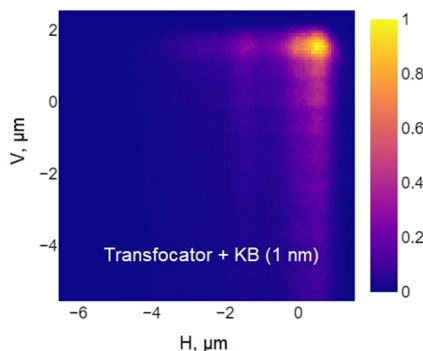


**FIG. 27.** Source image calculated for the third undulator harmonic at 52 m from the source with focusing by KB mirrors of radiation prior collimated by transfocator. Intensity is given in relative units. The calculations were performed using the Shadow software and do not take into account possible coherence effects that can result in the appearance of diffraction-induced features in the beam.

For the third harmonic, at 52 m from the source  $t_c^{(t)}$  equals to  $\sim 260 \mu\text{m}$ , which is significantly less than the effective apertures of KB mirrors (825  $\mu\text{m}$ ) and CRLs of final focus (880  $\mu\text{m}$ ). With focusing in 1:1 ratio or collimation with transfocator, the transverse coherence length at 26 m from the source is twice less—130  $\mu\text{m}$ . For higher harmonics,  $t_c^{(t)}$  is lower than all mentioned apertures altogether. We find that such coherence level is high enough to add some structure to the intensity profiles calculated by ray-tracing but not enough to greatly change the overall beam shape and intensity distribution across the focused beam spot.

## V. END-STATION

The principal configuration of the experimental end-station is presented in Fig. 28. There are two places for samples: at distances (a) 42–49 m and (b) 52 m from the radiation source.

The following beam forming methods are available at distances of 42–49 m by using the transfocator, DMM and QCM:

- radiation with “natural” divergence (with transfocator removed from the beam);
- radiation collimated by transfocator;
- converging beams (transfocator at 26 m from the source work in the 1:1 focusing mode).

At 52 m from the source, the transfocator, DMM, QCM, and final focusing optics (CRLs and KB mirrors) will provide:

- radiation with “natural” divergence (with transfocator removed from the beam);

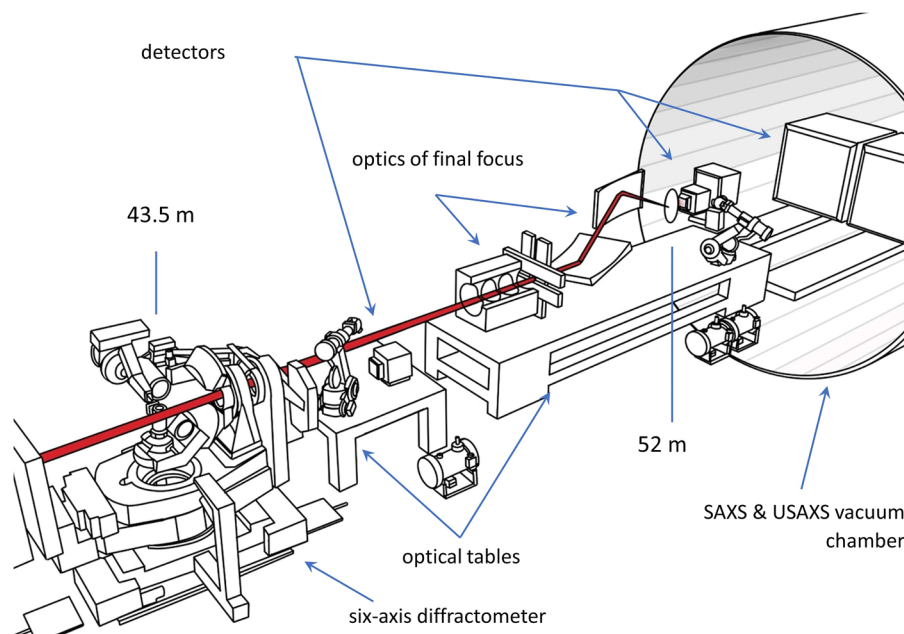


FIG. 28. Principal scheme of sample environments installation.

- radiation collimated by transfocator;
- beams focused by transfocator 1:1;
- beams focused by CRL 25:1;
- beams collimated by transfocator and focused by CRL;
- beams focused by KB mirrors 100:1 (possibly 150:1);
- beams collimated by transfocator and focused by KB mirrors.

In both cases, it is possible to have monochromatization as follows:

- using DMM with  $dE/E = 1 \times 10^{-2}$  (operating energy range: 10–30 keV);
- using DMM with  $dE/E = 4.6 \times 10^{-2}$  (operating range: 15–25 keV);
- using DMM and QCM with  $dE/E = 1.3 \times 10^{-4}$  (operating range: 10–30 keV).

At 42–45 m from the radiation source, it is planned to install a diffractometer based on a multifunctional, six-axis kappa diffractometer for crystallographic studies; and, at 45–47 m, a two-m-long optical table for various sample environment systems and detectors. Using relatively wide (not focused) beams, it will be possible to perform diffraction experiments with monochromatic and “pink” beam, diffraction in grazing incidence geometry, energy dispersive diffractometry, XRF and XAFS spectroscopy, and various types of x-ray imaging.

At 52 m from the source, the beamline is supposed to operate as virtually a “materials science microscope,” i.e., a set of monochromatic and “pink” beams with characteristic sizes ranging from 100 nm up to 1 mm pointing to the same position at the sample will be available. Optics of final focus, slits, sample manipulators and positioners, detectors for WAXS, x-ray imaging, XRF, and XAFS spectroscopy, as well as a robotic manipulator for a quick change

or replacement of detectors will be installed on a 4-m-long optical table. It is also planned to have specialized devices for mechanical and thermal treatments of the sample, as well as other user-provided apparatus, on this optical table. For SAXS and USAXS experiments, an evacuated chamber (i.e., the flight path tube under the modest vacuum,  $10^{-4}$ – $10^{-3}$  mbar) with a diameter of 1.5–2 m and a length of up to 25 m (in analogy with Ref. 20) will be located behind the optical table. Here, it is planned to install two detectors, inside the vacuum chamber, on independent rails covering half of the space behind the sample. In this case, a combination of WAXS, SAXS, and USAXS as well as other experimental methods utilizing coherence, e.g., ptychography, will be realized.

## VI. CONCLUSIONS

In materials science, it is essential to study matter at different structural levels: from surfaces, interfaces, and grains to their agglomerations and a whole bodies. Once we get down to the nanometer scale, it is important to make sure that we are exploring the same area (region of interest) in the sample. This is especially true for the characterization of *in situ* processes. These basic requirements are fulfilled by the presented beamline conceptual design. Namely, the following objectives have been addressed and achieved:

- Flexible beamline design for different experimental methods.
- Appropriate spatial resolution and high temporal resolution for *in situ* and *operando* research.
- Model of a “Materials science microscope” with a high variety of focusing modes.

We believe that our ideas and technical solutions, which we found and presented here, will be of a great interest for others developing and designing similar instruments around the world.

## AUTHOR DECLARATIONS

## Conflict of Interest

The authors have no conflicts to disclose.

## Author Contributions

**Vladimir A. Chernov:** Conceptualization (lead); Investigation (lead); Methodology (equal); Supervision (lead); Writing – original draft (equal); Writing – review & editing (equal). **Ivan A. Bataev:** Conceptualization (equal); Funding acquisition (equal); Resources (equal); Writing – original draft (equal). **Yakov V. Rakshun:** Conceptualization (lead); Project administration (lead); Supervision (lead); Writing – original draft (equal); Writing – review & editing (equal). **Yuri V. Khomyakov:** Data curation (lead); Investigation (equal); Software (lead); Visualization (lead); Writing – original draft (equal). **Maksim V. Gorbachev:** Investigation (equal); Software (equal); Visualization (equal); Writing – original draft (equal). **Andrei E. Trebushinin:** Data curation (lead); Investigation (equal); Visualization (lead); Writing – original draft (equal). **Nikolay I. Chkhalo:** Investigation (equal); Methodology (equal); Visualization (equal). **Dmitry A. Krasnorutsky:** Software (equal); Visualization (equal). **Viktor S. Naumkin:** Software (equal); Visualization (equal). **Artem N. Sklyarov:** Data curation (equal); Software (equal); Visualization (equal); Writing – original draft (equal). **Nikolay A. Mezentsev:** Conceptualization (equal); Supervision (equal); Validation (equal). **Alexander M. Korsunsky:** Conceptualization (equal); Supervision (equal); Writing – review & editing (lead). **Igor P. Dolbnya:** Conceptualization (lead); Methodology (equal); Supervision (lead); Writing – original draft (lead); Writing – review & editing (lead).

## DATA AVAILABILITY

The data that support the findings of this study are available from the corresponding author upon reasonable request.

## REFERENCES

- <sup>1</sup>J. Wright, C. Giacobbe, and M. Majkut, *Curr. Opin. Solid State Mater. Sci.* **24**(2), 100818 (2020).
- <sup>2</sup>U. Johansson, U. Vogt, and A. Mikkelsen, *Proc. SPIE* **8851**, 88510L (2013).
- <sup>3</sup>R. D. dos Reis *et al.*, *J. Phys.: Conf. Ser.* **1609**, 012015 (2020).
- <sup>4</sup>C. Reinhard, M. Drakopoulos *et al.*, *J. Synchrotron Radiat.* **28**, 1985–1995 (2021).
- <sup>5</sup>A. Trebushinin, S. Serkez, M. Veremchuk, Y. Rakshun, and G. Geloni, *J. Synchrotron Radiat.* **28**, 769 (2021).
- <sup>6</sup>G. Baranov, A. Bogomyagkov, S. Sinyatkin, and E. Levichev, “Lattice optimization of the Novosibirsk fourth-generation light source SKIF,” [arXiv:2107.03081](https://arxiv.org/abs/2107.03081).
- <sup>7</sup>T. Tanaka, *J. Synchrotron Radiat.* **28**, 1267 (2021).
- <sup>8</sup>See <https://www.rxoptics.de/products/lenses/> for information on refractive X-ray lenses.
- <sup>9</sup>M. Sanchez del Rio, N. Canestrari, F. Jiang, and F. Cerrina, *J. Synchrotron Radiat.* **18**, 708–716 (2011).
- <sup>10</sup>M. Svechnikov, *J. Appl. Crystallogr.* **53**(1), 244 (2020).
- <sup>11</sup>M. Sánchez del Río and R. J. Dejus, *Proc. SPIE* **8141**, 814115 (2011).
- <sup>12</sup>P. Brumund, J. Reyes-Herrera, C. Morawe *et al.*, *J. Synchrotron Radiat.* **28**, 1423 (2021).
- <sup>13</sup>Y. Li, A. M. Khounsary, J. Maser, and S. Nair, “Cooled mirror for a double-undulator beamline,” *Proc. SPIE* **5193**, 204 (2004).
- <sup>14</sup>L. Zhang, W.-K. Lee, M. Wulff, and L. Eybert, *J. Synchrotron Radiat.* **10**, 313 (2003).
- <sup>15</sup>Y. Touloukian, R. Powell, C. Ho, and P. Klemens, *Thermal Conductivity—Nonmetallic Solids, Thermophysical Properties of Matter Vol. 1* (IFI/Plenum, 1970).
- <sup>16</sup>T. Middelman, A. Walkov, G. Bartl, and R. Schödel, *Phys. Rev. B* **92**, 174113 (2015).
- <sup>17</sup>H. Watanabe, N. Yamada, and M. Okaji, *Int. J. Thermophys.* **25**(1), 221 (2004).
- <sup>18</sup>See <https://www.j-tec.co.jp/english/optical/high-precision-x-ray-mirror/> for information on high-precision x-ray mirrors.
- <sup>19</sup>P. Willmott, *An Introduction to Synchrotron Radiation. Techniques and Applications* (Wiley, 2019).
- <sup>20</sup>T. Narayanan, M. Sztucki, T. Zinn, J. Kieffer, A. Homs-Puron, J. Gorini, P. Van Vaerenbergh, and P. Boesecke, *J. Appl. Crystallogr.* **55**, 98 (2022).
- <sup>21</sup>T. E. J. Moxham *et al.*, *Appl. Phys. Lett.* **118**, 104104 (2021).
- <sup>22</sup>D. Laundry *et al.*, *Optica* **6**, 1484–1490 (2019).
- <sup>23</sup>A. Bragin, A. Zorin, S. Khrushev, V. Lev, N. Mezentsev, V. Shkaruba, V. Syrovatin, O. Tarasenko, V. Tsukanov, and A. Volkov, *IEEE Trans. Appl. Supercond.* **28**, 4101904 (2018).